Experimental Realization of Highly Efficient Beam Combination and Steering via Topological Multimode

Yuhao Jing, Yucong Yang, Weihan Long, Tianchi Zhang, Di Wu, Junxian Wang, Zhongfei Xiong, Nuo Chen, Mudi Wang, Che Ting Chan, Yu Yu, Lei Bi,* and Yuntian Chen**

Topology multimode provides a promising avenue for developing multi-channel robust photonic devices and optical power manipulation. Particularly, the backscattering-immune property of topological multimode holds potential for ideally lossless optical beam combination. In this work, the combination of topological multimode in topologically non-trivial photonic crystals, is experimentally observed achieving a beam combination efficiency of up to 93%. The near-perfect combination can be explained by the power orthogonal excitation principle of topological multimode. Furthermore, controllable beam steering is successfully achieved by incorporating topological one-way large-area waveguide states into the output spatial channel with tunable excitation. The work paves the way for the application of topological photonics in the directional manipulation of high-power electromagnetic radiation.

1. Introduction

In recent years, the interplay between topology and optics offers a promising route[1–18] for developing robust optical devices. For instance, optical isolators and topological lasers benefit from the unidirectional and backscattering-immune properties of the topological edge states. Additionally, a complex scenario that a system featuring several edge states,[14,15,19,20] referred to as topological multimode, can support a higher mode density, which provides opportunities for improved communication capacity,[21,22] and also suggests the possibility of novel topological devices for power manipulation. The original proposal for the multimode topological waveguides[14] theoretically proposed that the topological multimode could be achieved by gapping multiple Dirac and quadratic points, which has been experimentally demonstrated,[15,23] further indicating the feasibility of topological beam splitters.[23,24] Notably, the topological multimode have also been theoretically examined in-depth in the context of quantum electrodynamics, toward spontaneous entanglement generation using different topological channels.[19] Meanwhile, multifrequency and multimode topological waveguides have been proposed and experimental demonstrated for efficient and high-capacity optical transmission/communication devices.[25] Very recently, a study[20] elucidated the fundamental mechanisms underlying controllable multimode interference in the topological heterostructure, hence the experimental realization of controllable power splitting. Despite the significant efforts that have been devoted to theoretical development or understanding the underlying principles of topological multimode phenomena, the practical applications have been much more scarcely explored in literature.

Thanks to the inherent backscattering immunity, topological multimode waveguides are ideal for realizing beam combination. Beam combination deals with multiple beams of electromagnetic waves, typical laser light, in a way that allows for precise control over the intensity, direction, and shape of the resulting beams.[26,27] Such technology of controlling power intensity and direction of electromagnetic radiation is a demanding technology, and shows great advantage for many applications, including laser particle accelerators,[28–33] advanced materials processing,[34–37] and medical treatment.[38] Notably, the power scaling of the single laser systems has encountered

Y. Jing, Z. Xiong, N. Chen, Y. Yu, Y. Chen
School of Optical and Electronic Information
Huazhong University of Science and Technology
Wuhan 430074, China
E-mail: yuyu@mail.hust.edu.cn; yuntian@hust.edu.cn

Y. Yang, W. Long, T. Zhang, D. Wu, J. Wang, L. Bi
National Engineering Research Centre of Electromagnetic Radiation Control Materials
University of Electronic Science and Technology of China
Chengdu 610054, China
E-mail: bilei@uestc.edu.cn

Y. Yang, W. Long, T. Zhang, D. Wu, J. Wang, L. Bi
State Key Laboratory of Electronic Thin-Films and Integrated Devices
University of Electronic Science and Technology of China
Chengdu 610054, China

M. Wang, C. T. Chan
Department of Physics
The Hong Kong University of Science and Technology
Hong Kong 999077, China

Y. Yu, Y. Chen
Wuhan National Laboratory of Optoelectronics
Huazhong University of Science and Technology
Wuhan 430074, China

Y. Yu, Y. Chen
Optics Valley Laboratory
Wuhan 430074, China

The ORCID identification number(s) for the author(s) of this article can be found under https://doi.org/10.1002/lpor.202401157

DOI: 10.1002/lpor.202401157

several physical limitations,[39–41] thus beam combination of multiple output power of laser systems has been the first measure to boost the power level. As for continuous waves, beam-combining technology can be categorized into coherent or incoherent beam combinations. The coherent beam combination essentially relies on the carefully delayed and locked phase of each combination channel for either tiled aperture or filled aperture geometries to maintain mutual coherence in both space and time.[42–49] For monochromatic incoherent beam combinations, the passive combiner, such as polarization beam splitters,[50] has a very limited number of input channels that maintain power orthogonality. In this regard, it is important to develop a beam combination strategy that can operate without complicated feedback and simultaneously admit multiple input channels.

In this work, we theoretically proposed and experimentally realized highly efficient beam combination and steering via topological multimode. Although beam combination can be regarded as the inverse process of beam splitting as elaborated through multimode interference,[20] we instead discover that the interference terms disappear here, which is coined as power orthogonal excitation principle in topological beam combination. Importantly, power orthogonal excitation principle promises for the robust power manipulation, i.e., termed as topology-enabled beam combination (TEBC) and topology-enabled beam steering (TEBS) in this paper. Specifically, we design and fabricate a 3×1 combiner with an experimental TEBC efficiency of up to 93%. We further implement TEBS by incorporating multi-topological one-way large-area waveguide states (TOLWSs)[51] into the output spatial channel, akin to an optical phased array. We show that the controlled beam steering could be realized through properly engineering mode profiles of multi TOLWSs by excitation condition adjustment or frequency sweep. The manipulation of topological multimode shows potential advantage of experimental simplicity, leading to smaller main lobe width and suppressed side lobe for beam steering due to expanded modal area in the near field, as verification in numerical simulation with 3×1 combiner and experimental measurement with 5×1 combiner, which pave the way for practical applications to directionally manipulate high-power electromagnetic energy radiation.

2. Results and Discussion

2.1. Beam Combination Model Based on Spiral-Staircase Topology

In topology-related physics, a significant result is the existence of gapless edge states localized at the interface as the topological invariant of two neighbor bulk materials changes. In 2D systems, the topological invariant is usually coined as Chern number and calculated by integrating Berry curvature over the entire 2D Brillouin zone.[52,53] Implied by the stability of the topology associated with the Bloch modes across the entire Brillouin zone, the chiral edge state is robust against small perturbations, i.e., without closing or opening the bandgap. In the topological scenario, the broken of time-reversal symmetry at the Dirac point brings a massive Dirac Hamiltonian, $\mathbf{H}\,(k) = \hbar v_F k \cdot \sigma + m\sigma_z$, where the mass term m flips sign across two topologically different bulk materials.[54] At the interface, $\mathbf{H}(k)$ has an elegant stationary solution given by $E\,(k_x) = \hbar v_F k_x$, where group velocity $v_F = 1/\hbar \cdot dE/dk_x$ and the sign of v_F determines the chirality of edge states. Although $E(k_x)$ could develop a kink, the number of edge states is fully determined by the topological structure of the bulk states, which has been dictated by the bulk-boundary correspondence. Specifically, the gap Chern numbers of two neighboring bulk photonic crystals are C_m and C_n respectively, the difference and its sign, i.e., $\Delta n = C_m - C_n$, essentially determines the number and propagation direction of edge states, as shown in **Figure 1a**.

The general principle of our TEBC via topological multimode is sketched in Figure 1b, which shows a spiral staircase distribution of gap Chern number of topologically different bulk materials, with a topological point junction in the center. Each stair interface plays the role of one input channel and only supports one chiral edge state propagating toward the topological point junction, while the cliff spatial channel acts as the output port, and supports n unidirectional edge states, constituting the topological multimode, propagating outward the topological point junction. The total input energy is forced to combine at the output port, as guaranteed by both the chirality of edge states and the law of energy conservation. More importantly, the topological property for scattering-free edge states renders the beam combination phase-insensitive. The number of beam combination channels is determined by the difference in the gap Chern number across the cliff interface. It shows the advantage against the incoherent beam combination between orthogonal polarized electromagnetic waves, which is usually limited to two channels.

2.2. Topologically Protected Power Orthogonal Excitation

The spatially overlapped topological multimode is the necessary condition to realize highly efficient beam combination, while the sufficient condition is the topologically protected unidirectionality of the propagating edge states spanning a high dimensional modal space in the topological point junction with energy conservation. Indeed, our proposal of efficient beam combination is due to energy conservation in the point junction with the topology-protected unidirectionality of those edge states. This leads to orthogonal excitation of topological multimode for among any input channel, which is coined "power orthogonal excitation". Namely, for a given source launched at any input channel i, the excited state ($\psi_i = \sum_n a_n \phi_n$, ϕ_n is the eigenmode profile of topological multi-edge states and a_n is the superposition factor) at the cliff interface, shall be orthogonal to that (ψ_j) of input channel j. The interference term in power basis between ψ_i and ψ_j is enforced to disappear under the principle of power orthogonal excitation.

A rigorous description of the power orthogonal excitation can be given using the optical scattering matrix, wherein the input and output channels are located at high dimensional modal space composed of topological multimode (Note S2, Supporting Information). The idea is to take the absence of the scattering channels to accomplish the dimensional reduction of the scattering matrix at the topological point junction where the beam combination occurs. Thus, the three edge states located at three separate spatial channels could be regarded as the input ports for the scattering matrix, while the output ports are three edge states lying on the same spatial, as shown in Figure 1c.

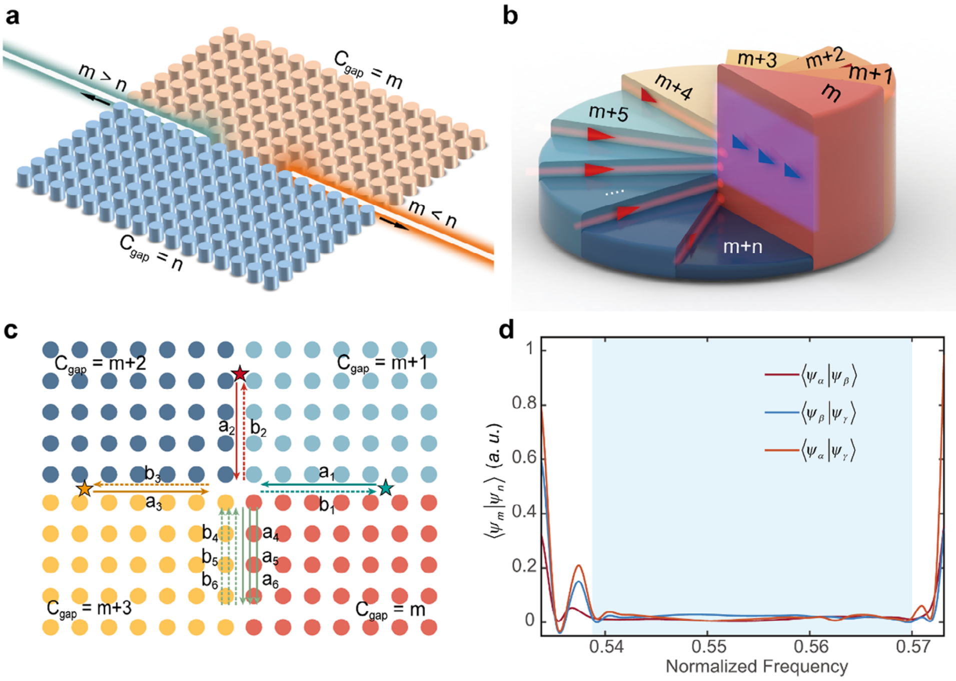

Figure 1. The spiral staircase distribution of Chern number and its power orthogonal excitation. a) The number and propagation direction of the edge states are determined by the absolute value and the sign of $C_m - C_n$ of two neighboring bulk materials, respectively. b) The spiral-staircase topology of gap Chern numbers with the fan-shaped distribution. Each sector with a gap Chern number indicated by the black/white number. At all stair interfaces, the edge states propagate inward, while the edge states propagate outward at the cliff interface. c) The 3×1 beam combiner with optical scatting matrix representation. The stars denote the electromagnetic wave sources. The solid arrows represent the topological protected edge states, while the dashed arrows are topological forbidden. d) Orthogonality of topological edge states. The three input modes are marked as ψ_α, ψ_β, ψ_γ, when only the dipole located at input left (green), top (red), or right (orange) spatial channel is active.

As for the 3×1 beam combiner, the three excited states are denoted as ψ_i, $i \in (\alpha, \beta, \gamma)$, where α, β and γ represents individual excitation from the three different input channels. The interference term in power basis between topological multimode can be described as follows (see Note S1, Supporting Information for the derivation),

$$\left\langle \psi_i \,\middle|\, \psi_j \right\rangle = \frac{\int \left(E_j \times H_i^* + E_i^* \times H_j\right)_y dl}{\sqrt{\int \left(E_i \times H_i^* + E_i^* \times H_i\right)_y dl \cdot \int \left(E_i \times H_i^* + E_i^* \times H_i\right)_y dl}} = \delta_{ij} \tag{1}$$

where $E_{i,j}$, $H_{i,j}$ are the electric and magnetic field components associated with the excited state $\psi_{i,j}$, δ_{ij} is the Kronecker symbol, and the line integral could be located at arbitrary cross-section perpendicular to the propagated direction. Three excited states are pairwise orthogonal, as evident from the projection $\langle \psi_i \mid \psi_j \rangle$ in the shared bandgap, as shown in Figure 1d. The power orthogonal excitation also indicates that the topological multimodes are mutually independent and thus fulfill the superposition principle in terms of optical power full rather than the optical field, which bears a resemblance to the incoherent beam combination between two orthogonal polarized light beams. Importantly, TEBC has no limit to the number of combining channels and is rooted in the orthogonality among topological multimode.

2.3. Experimental Implementation of the Spiral-Staircase Topology

The spiral-staircase topology for beam combination via topological multimode can be realized by arranging photonic crystal properly.[12,15] Generally, the large Chern number requires the participation of more pairs of Dirac points or quadratic points gapped by time-reversal symmetry breaking. Therefore, to illustrate the basic idea of the spiral-staircase topological device, we arrange four types of photonic crystal with different gap Chern numbers together, as shown in **Figure 2**a. The four various photonic crystals share a similar unit cell structure, which contains the yttrium iron garnet (YIG) rod sandwiched between two copper-clad laminates (CCLs, see Experimental Section for details) sketched in Figure 2b. Each YIG rod is biased by a NdFeB magnet-provided magnetic field (Note S3, Supporting Information). The magnetized YIG-based photonic crystal generates the complete bandgaps for TM polarization at microwave frequencies. Specially, we utilized 4 *mm* height YIG rods with the radius of r_1, r_2, r_3, and r_4 illustrated in Figure 2c to f to construct photonic crystals with different gap Chern numbers ($C_{gap} = -2$, $C_{gap} = -1$, $C_{gap} = 0$, $C_{gap} = 1$) in a frequency range of 8.95–9.45 GHz with overlapped bandgap (Note S4, Supporting Information).

We proceed to discuss the experimental realization of the TEBC by measuring the real-space field distribution,[55] as shown in **Figure 3**a. To probe the mode profile, we placed three coherent dipole antennas at three marked positions, and moved

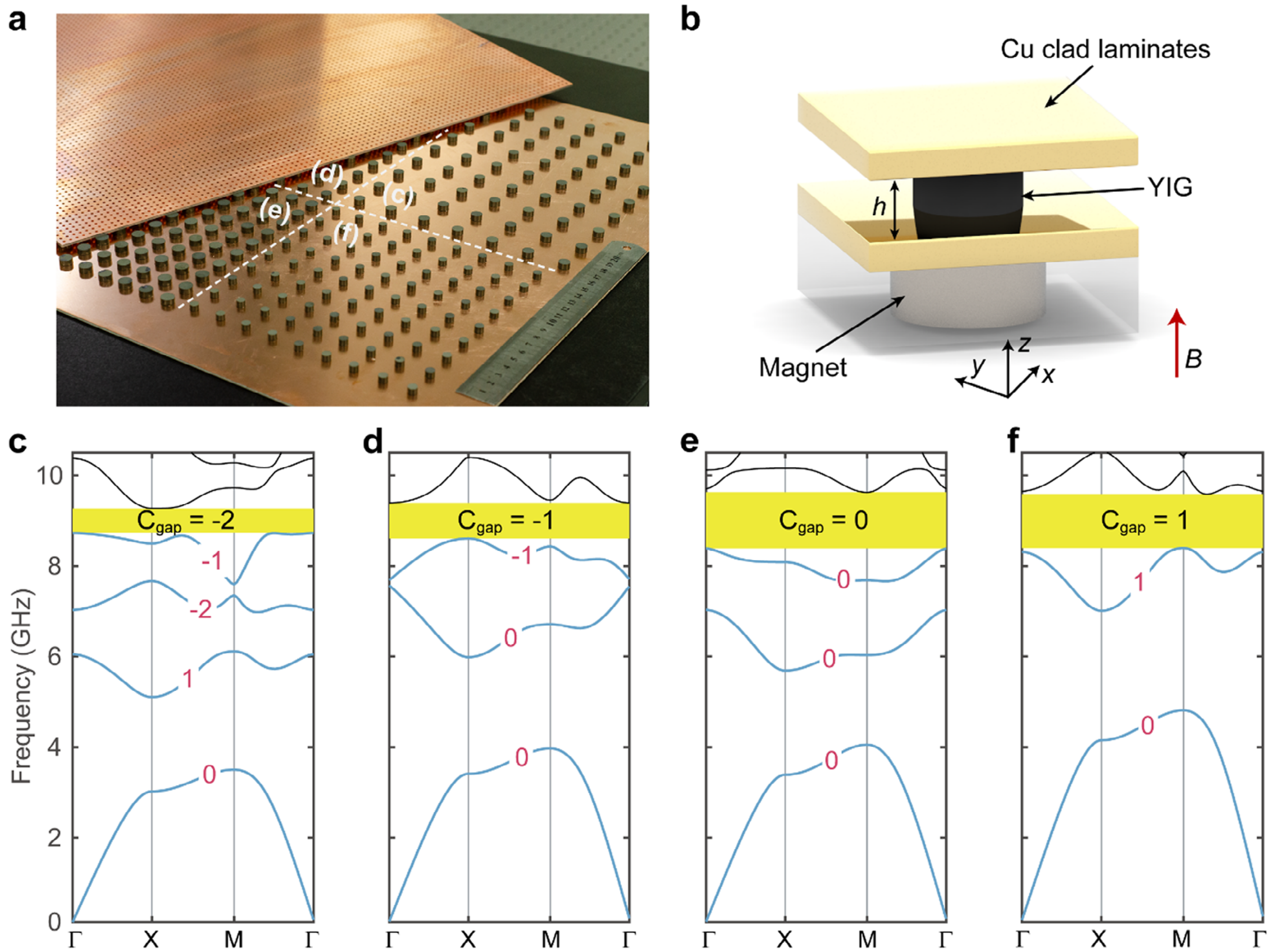

Figure 2. Topological non-trivial photonic crystals and band structures. a) Photonic crystal with YIG rods arranged in a square lattice with variable radius and lattice constant. b) The unit cell of the photonic crystal. c) to f) The complete photonic band structure for TM polarization. The Chern number of each band is indicated by the red number. The gap Chern number can be calculated by summing the Chern numbers of each band below the bandgap. Regions of bandgaps are highlighted in yellow.

the probe antennas to record the magnitude and phase of the electric field at each position (see Experimental Section for details). Figure 3b shows the measured distribution of E_z component at 9 GHz. We also measured the field profile for the input frequency range of 8–10 GHz. The edge states unidirectionally propagate along the interfaces between photonic crystals with different Chern numbers, preserving fairly good field confinement (see simulated mode profiles in Note S5, Supporting Information).

Figure 3c to f show the projected band structures obtained by converting the measured and simulated mode profile of the edge states from real space to k-space via discrete Fourier transform (FT) in a frequency range of 8–10 GHz. The peak location of the measured dispersion of the edge states matches perfectly well theoretically calculated results. The sign of group velocity for those edge states could be obtained from Figure 3c to f, indicating the unidirectional energy flow predicted in the spiral-staircase topology. Compared to the calculated band structure, the linewidth of the edge states from the experiment is wider, which is due to the measurement accuracy limited by the finite sampling (the lattice constant (5mm) of the holes array of the CCLs). The uncompleted bandgap and discontinuity of the experimentally measured edge state originated from fabrication-caused inhomogeneity of the applied magnetic field. The disconnected edge modes observed in Figure 3e are caused by the excitation probe used in the experiment, wherein the excitation efficiency is related to both the position of the excitation probe and the mode profile of edge states (see detailed discussion on disconnected edge modes in Section S4, Supporting Information).

2.4. Phase-Insensitive High Efficiency Beam Combination

In conventional beam combination optical systems, complicated feedback and optical structures have been adopted to build the phase correlation precisely between different input beams.[26,56] In contrast, the TEBC has no such need for controlling phases among different channels, thus showing certain advantages in

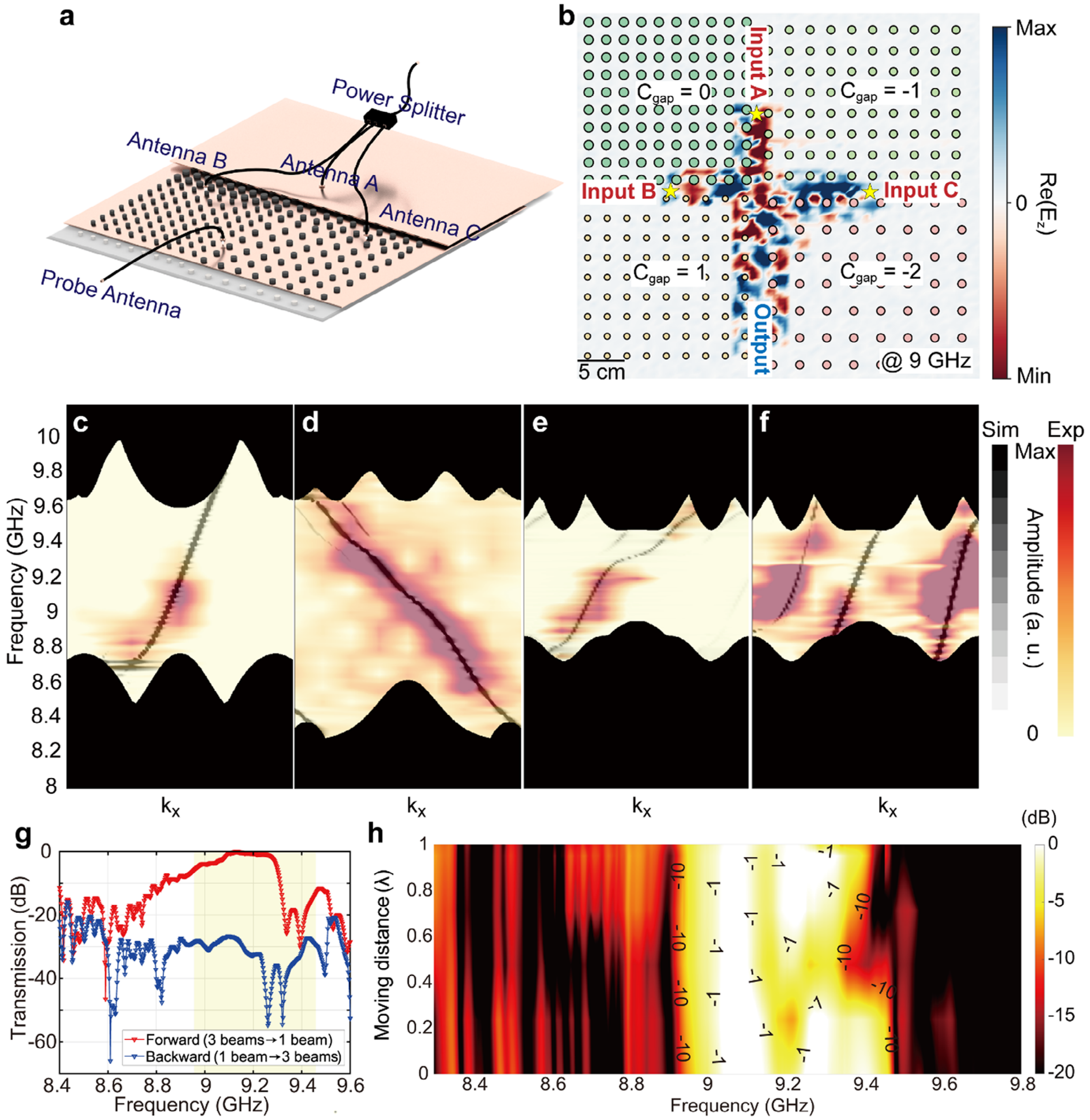

Figure 3. Experimental setup, measured field profile and the efficiency for beam combination. a) Schematic of the fabricated YIG photonic crystal sample. b) Measured $Re(E_z)$ distribution in the photonic crystal for three input sources at 9 GHz, demonstrating topology-enabled beam combination. The mode width of combined waves D is $\approx 1.44 * \lambda$. c) to f) The projected band for four spatial channels. The FT of mode profile directly demonstrate the dispersion of top ($C_{gap} = 0$ and $C_{gap} = -1$, Input A), left ($C_{gap} = 0$and $C_{gap} = 1$, Input B), right ($C_{gap} = -2$ and $C_{gap} = -1$, Input C) and bottom ($C_{gap} = -2$ and $C_{gap} = 1$, Output) spatial channels respectively. The FT from simulation and experiment data are emphasized by the dark-white color bar and red-yellow color bar separately. g) The experimental transmission spectra for forward (3 beams to 1beam) and backward (1 beam to 3 beams) propagation. h) Experimental transmission of forward as a function of the frequency and the moving distance of the dipole.

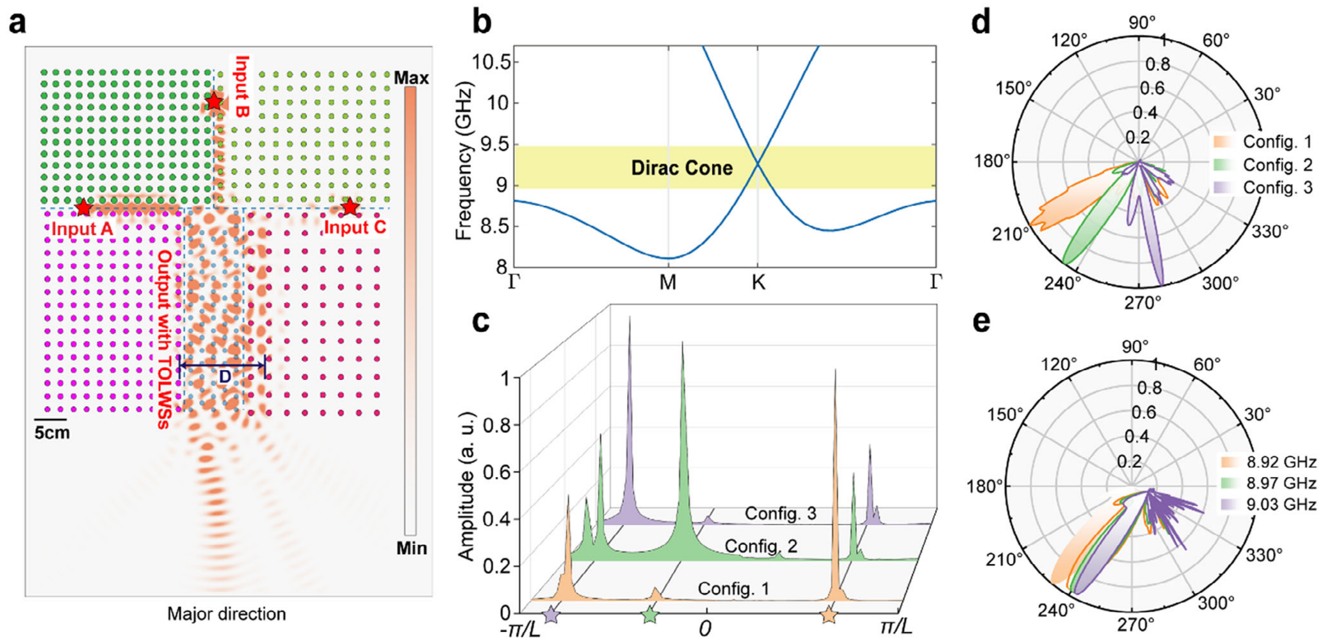

Figure 4. Selective excitation to realize beam steering in farfield. a) Simulated $|E_z|^2$ distribution with TOLWSs at 9 GHz, demonstrating topology-enabled beam steering in near-field. The mode width of combined TOLWSs D is $\approx 4.20 * \lambda$. b) The band structure of photonic crystal embedded in output spatial channel with Dirac cone. c) The spectrum contents and d) corresponding farfield patterns of the three excited TOLWSs. L is the lattice constant of sandwiched hexagonal photonic crystal. e) Frequency-angular beam steering using TOLWSs in topological multimodal space.

terms of simplicity and efficiency. Next, we discuss the efficiency of topology-enabled beam combination. To that end, we fix the position of the probe antenna for the output channel and measure beam combination efficiency against the variation of 1) the operation frequency and 2) the position of excitation antennas (see Experimental Section; Note S6, Supporting Information for details).

We first measured the beam combination efficiency as a function of the operation frequency. The yellow region in Figure 3g represents the overlapped bandgap region of the four photonic crystals. Inside the yellow region, all the edge states exhibit strong unidirectionality. As for the forward propagating states (labeled in red line), the beam combination shows high transmission in the bandgap frequency range. Whereas the backward propagation (labeled in blue line) loss is in-between 20 and 55 dB, indicating that the backward propagating state is forbidden. At the frequency of 9.12 GHz, the forward transmission loss at the output port is −0.31 dB, which is primarily due to the material absorption of YIG. The calibration procedure has been adopted to eliminate the losses from the power splitter, cables, connectors, and excitation, ensuring the reported transmission reflects the performance of the topological waveguide itself rather than artifacts of the measurement system (see detailed calibration procedure in Note S6, Supporting Information). In the frequency range of 9 to 9.1 GHz which is close to the bulk band, the transmission is slightly dropped since the excitation efficiency is not exactly 100%. In the frequency region between 9.25 and 9.45 GHz, beam combination efficiency drops significantly due to the inhomogeneity of the applied magnetic field, leading to a narrower bandgap than that used in the simulation (see details in the Note S7, Supporting Information).

We further measured beam combination efficiency as a function of the operation frequency and the position of the excitation antenna as plotted in Figure 3h, wherein the coordinate of the excitation antenna varies from 0 to 7 cm ($\lambda = 7$ cm is the vacuum wavelength at 9 GHz). In the frequency range of 8.98–9.25 GHz, the transmission loss is lower than −1 dB. The variation of transmission loss is below 0.8 dB as the dipole antenna moved across a whole wavelength at 9.1 GHz. Remarkably, the variation of the position of the excitation antenna will change the phase correlation among three input edge states at the topological point junction, wherein the high efficiency of beam combination outright demonstrates topologically protected phase-insensitivity.

2.5. Directional Emission and Beam Steering

Achieving long-range and high-resolution light detection and ranging (LiDAR) requires flexible beam steering and collimation, while direct waveguide facet coupling to free space from the aforementioned beam combiner leads to wide main lobe with multiple side lobes (Note S8, Supporting Information), which undermines the practical applications of the proposed TEBS.

To overcome this problem, we proposed a strategy that could be analogy to phased array arranged in topological multimodal space by introducing a sandwiched photonic crystal in-between two domains of magnetic photonic crystals at output spatial channel in our beam combiner, as shown in **Figure** 4a,b. Such type of heterostructure permits TOLWSs in the TEBC operating frequency range (Note S9, Supporting Information), which facilitates one-way wave transport over a large mode width ($D \approx 4.20 * \lambda$), enabling the output spatial channel to carry a significant amount

Table 1. Relative amplitudes and phases of the input sources A–C.

	Relative Amplitude of Input Sources A–C	Relative Phases of Input Sources A–C
Config. *1*	$I_A^1, 0.07 * I_A^1, 0.04 * I_A^1$	$(0, -0.15\pi, 0.15\pi)$
Config. *2*	$(0, 0, I_A^2)$	$(0, 0 * P_C^2, P_C^2)$
Config. *3*	$(I_A^3, 2.59 * I_A^3, 0.99 * I_A^3)$	$(P_A^3, P_A^3 + 0.10\pi, P_A^3 - 1.21\pi)$

of energy without overheating the device. This stands in stark contrast to edge states found in previous structure, which are limited to small spatial regions ($D \approx 1.44 * \lambda$). The sandwiched triangular-lattice photonic crystals work as a bulk material to provide Dirac cone dispersion, so that the lattice mismatch only changes the mode profile but does not harm the power orthogonal excitation on the multimode output channel. Moreover, the TOLWSs bring superior collimation in farfield than that in the original edge-mode structure, as the beam width of main lobe is inversely proportional to the width of the mode profile in near-field. The overall transmission in coupled topological valley waveguide has been reported to be sensitive to the coupling between parallel topological valley edge states.[57] Thanks to the time-reversal symmetry breaking and spatial staircase topology in our scenario, the efficient beam combination still holds no matter whether the coupling condition between the input and output channels changes. The excitation ratios among the output multi-modes crucially depend on the excitation conditions. As a very typical example, it is possible to find a specific configuration of excitation condition to independently excite different edge states on the multimode output channel. Consequently, spatial beam collimation and steering (named "K-steering") can be conveniently achieved in topological multimodal space, i.e., selective excitation of TOLWSs, which is similar to a specific configuration of phased array. Although the exited states, the superposition of multi TOLWSs, are pairwise orthogonal in power basis, its mode profiles can still be engineered by tunable excitation. Figure 4c,d show Bloch-wavevector spectra and the corresponding farfield patterns of the excited states, which are coded in yellow, green, and violet color, respectively. The three TOLWS modes can be individually excited in the topological multimodal space by selecting proper amplitudes and phases of among the input sources labeled by "Config. i" ($i \in (1, 2, 3)$), the values of which are searched using particle swarm optimization procedure and tabulated in **Table 1** (Note S10, Supporting Information). For instance, with excitation condition given by Config. *3*, we show that the combined near-field electromagnetic wave are dominated by the Bloch-wave vector $\approx -0.78\pi/L$ (indicated by violet star in Figure 4c), which yields a narrow beam due to relative concentrated wave vectors[58] of the excited TOLWSs and larger D. Besides the discrete beam steering arising from topological multimodal space via engineered excitation in our TEBS structure, frequency also provides alternative degree of freedom to realize beam steering due to the relatively large bandgap at operation wavelength. As depicted in Figure 4e, we show that frequency-angular beam steering (named "F-steering") is applicable in our TEBS under the scheme of frequency-angular phased array in topological multimodal space with steering ability is $\approx 3.55°$ per 0.1 GHz, which shows potential application in non-mechanical beam steering LiDAR.

We also implemented TEBC and TEBS using a cascaded spatial staircase configuration (see Note S11, Supporting Information) as shown in **Figure 5a**. The measured beam combination efficiency of the TEBC, presented in Figure 5b, indicates that the combining efficiency of the cascaded configuration varies with frequency and phase difference. Specifically, the phase of source B varies from 0 to 2π, while the phases of other sources remain constant. This setup demonstrates significant combining performance within the frequency range of 8.75 to 9.12 GHz, encompassing the shared topologically non-trivial bandgap. By arranging the appropriate relative amplitudes and phases of the input sources, we experimentally measured the near-field distribution and obtained the far-field patterns of normalized electric fields by FT, as shown in Figure 5c to e, illustrating the scenario of K-steering. Concurrently, Figure 5f presents experimental results of F-steering, achieved by setting different frequencies under the same excitation configuration.

3. Conclusion

We propose the concept of TEBC and TEBS and design a compound structure with spiral-staircase topology, to realize efficient beam combination and steering via topological multimode. The proof-of-concept of TEBC has been verified in both numerical simulation and experimental measurement, showing beam combination efficiency upper to 93% over a broad frequency range of 9.1–9.3 GHz, which is useful in long-distance wireless energy transmission and high-power radar. From the viewpoint of classical electromagnetics, we proposed the concept of power orthogonal excitation principle, wherein multiple spatial overlapped yet power orthogonal channels can be handled as the basis of topological multimodal space. The interference between excited states, the superposition of topological multimode, disappear in the context of power basis. By engineering the mode profiles of TOLWSs, we further demonstrate the effectiveness of TEBS through selective excitation and frequency regulation. We employ a heterostructure to broaden edge state patterns in near-field, leading to narrower main lobe widths in farfield radiation. Our proposed TEBC and TEBS methods hold promise in the manipulation of high-power electromagnetic energy radiation with enhanced directionality. Another general high efficiency excitation approach from waveguide modes to topological edge states has been reported at microwave frequency via mode profiled matching,[59] which significantly benefits the practical application of the beam combiner for high power lasing. Compared to coherent LiDAR with optical phased arrays for beam steering, our solution manipulates light beam with the freedoms of TOLWS modes and frequency and may promise to reduce system complexity.

As a side remark, the topological point junction arising from the spatial stair-case topology does not have any well-defined interface, thus conventional bulk-boundary correspondence is not applicable here. Notably, the topological point junction leads to topologically protected power orthogonal excitation, and is distinguished from the singularity in real space, such as the dislocation and the disclination in crystal. As an outlook, the operating

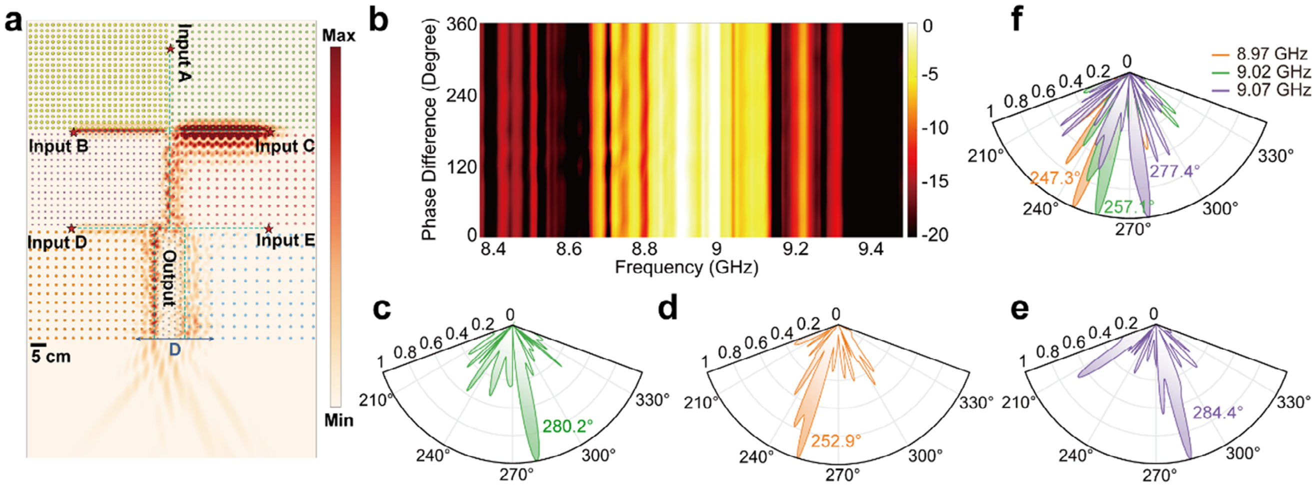

Figure 5. Experimental implement of TEBC and TEBS with cascaded spatial stair-case configuration. a) Simulated $|E_z|$ distribution with TOLWSs at 9.02 GHz. The mode width of combined TOLWSs D is $\approx 7.39 * \lambda$. b) The measured beam combination efficiency varies with the frequency and phase difference. The farfield patterns of normalized electric fields with phase configurations (P_A, P_B, P_C, P_D, P_E) are c) ($1.55\pi, 0.46\pi, 0.90\pi, -1.14\pi, 0$), d) (0, 0, 0, 0, 0), and e) ($0.57\pi, -1.14\pi, 1.25\pi, 0.66\pi, 0$). The amplitudes of all sources are set to be equal. f) Experimental measurement of "F-steering" with phase configuration (0, 0, 0, 0, 0).

frequency of TEBC and TEBS can also be extended to optical and telecommunication frequencies. For on-chip integrated, efficient beam combination and steering, we can use yttrium iron garnet thin films with permittivity tensors such as cerium or bismuth-doped yttrium iron garnet, which can be monolithically deposited on silicon or silicon nitride substrates to form TE-mode photonic crystals,[60,61] which can be demonstrated by careful design and continuous material improvement. The TEBC and TEBS devices via topological multimode offer a route for developing practical applications of topological photonics.

4. Experimental Section

Device Fabrication: Topology-enabled beam combination device was composed of square arrays of YIG pillars with different radius and lattice constants, sandwiched in between two 500 × 500 mm copper-clad laminates (CLLs). The radiuses of the four photonic crystals are 4.172, 4.054,4.748, and 3.038 mm respectively, and the corresponding lattice constants are 2.781, 2.145, 1.805, and 2.025 cm, and all YIG pillars were set to 4 mm in height to match the distance between CLLs (as shown in Figure 2a). The radiuses of added photonic crystals used in 5 × 1 combiner are 3.931 and 4.172 mm, and the corresponding lattice constants are 3.639 and 2.781 cm. The two CCLs were placed face-to-face and used as the reflectors to form a Fabre-Polar cavity. In the plane, photonic crystal arrays were placed in the same pattern as sketched in Figure 2a, leading to four interfaces separating four topologically different bulk materials. YIG pillars were made of YIG block crystal using ultra-high precision computer numerical control (CNC) machine (Mazak variaxis i700), with a processing error of less than 0.05 mm. In order to firmly fix the YIG pillars on the copper-clad laminated substrate, double-sided tape was first applied to the bottom side of YIG pillars. Subsequently, each YIG pillar was aligned with precisely defined acrylic mold with a holes array, the radius, lattice constant and height have one-to-one corresponded to that of YIG pillars). After pressing the YIG pillars with double-sided and accurately fixing the YIG pillars onto the CCL bottom plate through the mold, the acrylic mold was carefully removed to prevent damage to the YIG pillars.

First, a 2 mm thick acrylic plate with double-sided tape was set to form the substrate, which was used to align the NdFeB magnets accurately underneath each YIG column, and to make sure appropriate magnetization of each YIG pillar. Then, a 5 mm thick acrylic mold with precisely defined configuration was fixed on the prepared substrate. At last, the NdFeB magnets were settled in the holes array of the 5 mm thick acrylic plate with the same direction, which provides the applied magnetic field.

Characterization Setup: Four antennas setup was used, i.e., three dipole antennas as the transmitter and one dipole antenna as the receiver, to characterize the samples. The input electromagnetic wave was connected to a MNK Communication power splitter (Working Freq: 5–10 GHz) through a coaxial cable. The input electromagnetic wave was divided into three coherent electromagnetic waves of the same frequency, while the output electromagnetic wave was received by the probe dipole antenna. The projected band structure, transmission spectra, and near-field distribution of the proposed TEBC device were measured using the four antennas setup. The four antennas were inserted into the waveguide through holes drilled with an ultra-high precision CNC machine and connected to the vector network analyzer (rod and Schwartz ZNB 20) to measure S-parameters. In all the measurements, the 3.5 mm 85052D through-off-short-match (TOSM) calibration and short-circuit calibration of the dipole antenna were performed, hence the measured S-parameters only contain the insertion loss of the device.

The experimental setup for projected band measurement includes a vector network analyzer (VNA) connected to three excitation probes through a 1-to-3 power splitter and a scanning probe, which were used to excite and detect the system's response, respectively. The excitation probe was positioned at a fixed location to inject a microwave signal into the sample, while the scanning probe measured the transmission or reflection response at different spatial positions. The data was processed using Fourier Transform Field Scan (FTFS) techniques to reconstruct the projected band structures in momentum space. Impedance-matched loads were used to calibrate and ensure accurate measurements.

A stepper motor-driven near-field scanning system was employed to measure the near-field radiation patterns of the 5 × 1 combiner, and the farfield patterns of the normalized electric field were subsequently obtained through a 2D Fourier transform.

Numerical Simulation: The full-wave results of the band structures and mode profiles shown in Figures 2–4 are performed using the commercial finite element method software COMSOL Multiphysics, in which Electromagnetic waves, Frequency domain (EWFD) module was used to demonstrate topological non-trivial TM band structures. To calculate the Chern number of each band below the interest bandgap, a gauge-invariant numerical method has been adopted to calculate the band Chern number in the discretized Brillouin zone.

When calculating the mode profiles of the excited edge states, the magnetic dipoles were placed to excite edge states located at different spatial channels. Perfectly matched layer was used to properly truncate the simulation domain. 1D discrete Fourier Transform was adopted to produce the projected bands of edge states.

Supporting Information

Supporting Information is available from the Wiley Online Library or from the author.

Acknowledgements

Y.J. and Y.Y. contributed equally to this work. The authors are grateful for support by the National Natural Science Foundation of China (NSFC) (Grant Nos. 12274161, 61405067, U22A20148, 51972044, 52021001, and 52102357), the Ministry of Science and Technology of the People's Republic of China (MOST) (Grant Nos. 2021YFB2800303 and 2021YFB2801600), Sichuan Provincial Science and Technology Department (Grant No. 99203070), the Innovation Project of Optics Valley Laboratory, and the Hong Kong RGC (Grant AoE/P-502/20).

Conflict of Interest

The authors declare no conflict of interest.

Author Contributions

Y.C. performed in conceived the original idea and supervised the project, Y.J. performed in carried out the theoretical work under the guidance of Y.C., M.W., and C.T.C., Y.Y. and L.B. performed in designed the experiment, Y.Y., W.L., T.Z., D.W., and J.W. performed the experiment, Y.J., Y.Y., Y.C., and L.B. performed in analyzed the data, Y.J., Y.Y., Z.X., and N.C. performed in wrote the manuscript, Y.C., L.B., and Y.Y. performed in revised the manuscript.

Data Availability Statement

The data that support the findings of this study are available from the corresponding author upon reasonable request.

Keywords

beam combination, beam steering, power orthogonal excitation, topological multimode

Received: July 24, 2024
Revised: January 28, 2025
Published online: February 28, 2025

[1] L. Lu, J. D. Joannopoulos, M. Soljačić, *Nat. Photonics* **2014**, *8*, 821.
[2] A. B. Khanikaev, G. Shvets, *Nat. Photonics* **2017**, *11*, 763.
[3] T. Ozawa, H. M. Price, A. Amo, N. Goldman, M. Hafezi, L. Lu, M. C. Rechtsman, D. Schuster, J. Simon, O. Zilberberg, I. Carusotto, *Rev. Mod. Phys.* **2019**, *91*, 015006.
[4] M. Hafezi, E. A. Demler, M. D. Lukin, J. M. Taylor, *Nat. Phys.* **2011**, *7*, 907.
[5] M. Hafezi, S. Mittal, J. Fan, A. Migdall, J. M. Taylor, *Nat. Photonics* **2013**, *7*, 1001.
[6] A. B. Khanikaev, S. Hossein Mousavi, W.-K. Tse, M. Kargarian, A. H. MacDonald, G. Shvets, *Nat. Mater* **2013**, *12*, 233.
[7] G. Q. Liang, Y. D. Chong, *Phys. Rev. Lett.* **2013**, *110*, 203904.
[8] W.-J. Chen, S.-J. Jiang, X.-D. Chen, B. Zhu, L. Zhou, J.-W. Dong, C. T. Chan, *Nat. Commun.* **2014**, *5*, 5782.
[9] F. D. M. Haldane, S. Raghu, *Phys. Rev. Lett.* **2008**, *100*, 013904.
[10] S. Raghu, F. D. M. Haldane, *Phys. Rev. A* **2008**, *78*, 033834.
[11] Z. Wang, Y. D. Chong, J. D. Joannopoulos, M. Soljačić, *Phys. Rev. Lett.* **2008**, *100*, 013905.
[12] Z. Wang, Y. Chong, J. D. Joannopoulos, M. Soljačić, *Nature* **2009**, *461*, 772.
[13] K. Fang, Z. Yu, S. Fan, *Nat. Photonics* **2012**, *6*, 782.
[14] S. A. Skirlo, L. Lu, M. Soljačić, *Phys. Rev. Lett.* **2014**, *113*, 113904.
[15] S. A. Skirlo, L. Lu, Y. Igarashi, Q. Yan, J. Joannopoulos, M. Soljačić, *Phys. Rev. Lett.* **2015**, *115*, 253901.
[16] J.-W. Dong, X.-D. Chen, H. Zhu, Y. Wang, X. Zhang, *Nat. Mater.* **2017**, *16*, 298.
[17] T. Ma, G. Shvets, *New J. Phys.* **2016**, *18*, 025012.
[18] F. Gao, H. Xue, Z. Yang, K. Lai, Y. Yu, X. Lin, Y. Chong, G. Shvets, B. Zhang, *Nat. Phys.* **2018**, *14*, 140.
[19] C. Vega, D. Porras, A. González-Tudela, *Phys. Rev. Res.* **2023**, *5*, 023031.
[20] W. Tang, M. Wang, S. Ma, C. T. Chan, S. Zhang, *Light Sci. Appl.* **2024**, *13*, 112.
[21] L. G. Wright, F. O. Wu, D. N. Christodoulides, F. W. Wise, *Nat. Phys.* **2022**, *18*, 1018.
[22] C. Li, D. Liu, D. Dai, *Nanophotonics* **2019**, *8*, 227.
[23] M. Mehdipoura, M. Moeini, V. Ahmadi, R. Poursalehi, *Sci. Rep.* **2024**, *14*, 12905.
[24] M. Makwana, R. Craster, S. Guenneau, *Opt. Express* **2019**, *27*, 16088.
[25] B. Yan, Y. Peng, J. Xie, Y. Peng, A. Shi, H. Li, F. Gao, P. Peng, J. Jiang, J. Liu, F. Gao, S. Wen, *Laser Photonics Rev.* **2024**, *18*, 2300686.
[26] Z. Liu, X. Jin, R. Su, P. Ma, P. Zhou, *Sci. China Inf. Sci.* **2019**, *62*, 41301.
[27] P. F. McManamon, A. Ataei, *in Quantum Sensing and Nano Electronics and Photonics*, XVI, (Eds.: M. Razeghi, J. S. Lewis, G. A. Khodaparast, E. Tournié), SPIE, S. Francisco, U S, **2019**, p. 33.
[28] T. Tajima, J. M. Dawson, *Phys. Rev. Lett.* **1979**, *43*, 267.
[29] M. Roth, D. Jung, K. Falk, N. Guler, O. Deppert, M. Devlin, A. Favalli, J. Fernandez, D. Gautier, M. Geissel, R. Haight, C. E. Hamilton, B. M. Hegelich, R. P. Johnson, F. Merrill, G. Schaumann, K. Schoenberg, M. Schollmeier, T. Shimada, T. Taddeucci, J. L. Tybo, F. Wagner, S. A. Wender, C. H. Wilde, G. A. Wurden, *Phys. Rev. Lett.* **2013**, *110*, 044802.
[30] A. J. Kemp, S. C. Wilks, E. P. Hartouni, G. Grim, *Nat. Commun.* **2019**, *10*, 4156.
[31] W. Bang, B. J. Albright, P. A. Bradley, D. C. Gautier, S. Palaniyappan, E. L. Vold, M. A. S. Cordoba, C. E. Hamilton, J. C. Fernández, *Sci Rep.* **2015**, *5*, 14318.
[32] D. Mariscal, T. Ma, S. C. Wilks, A. J. Kemp, G. J. Williams, P. Michel, H. Chen, P. K. Patel, B. A. Remington, M. Bowers, L. Pelz, M. R. Hermann, W. Hsing, D. Martinez, R. Sigurdsson, M. Prantil, A. Conder, J. Lawson, M. Hamamoto, P. Di Nicola, C. Widmayer, D. Homoelle, R. Lowe-Webb, S. Herriot, W. Williams, D. Alessi, D. Kalantar, R. Zacharias, C. Haefner, N. Thompson, et al., *Phys. Plasmas* **2019**, *26*, 043110.
[33] A. Higginson, R. J. Gray, M. King, R. J. Dance, S. D. R. Williamson, N. M. H. Butler, R. Wilson, R. Capdessus, C. Armstrong, J. S. Green, S. J. Hawkes, P. Martin, W. Q. Wei, S. R. Mirfayzi, X. H. Yuan, S. Kar, M. Borghesi, R. J. Clarke, D. Neely, P. McKenna, *Nat. Commun.* **2018**, *9*, 724.
[34] JLMN **2017**, *12*, 3.

[35] JLMN **2018**, *13*, 3.
[36] F. Bauer, *JLMN* **2015**, *10*, 325.
[37] K. Bergner, M. Müller, R. Klas, J. Limpert, S. Nolte, A. Tünnerman, *Appl. Opt.* **2018**, *57*, 5941.
[38] R. Keenan, J. Dunn, P. K. Patel, D. F. Price, R. F. Smith, V. N. Shlyaptsev, *Phys. Rev. Lett.* **2005**, *94*, 103901.
[39] J. W. Dawson, M. J. Messerly, R. J. Beach, M. Y. Shverdin, E. A. Stappaerts, A. K. Sridharan, P. H. Pax, J. E. Heebner, C. W. Siders, C. P. J. Barty, *Opt. Express* **2008**, *16*, 13240.
[40] J. Zhu, P. Zhou, Y. Ma, X. Xu, Z. Liu, *Opt. Express* **2011**, *19*, 18645.
[41] J. Limpert, F. Stutzki, F. Jansen, H.-J. Otto, T. Eidam, C. Jauregui, A. Tünnermann, *Light Sci. Appl.* **2012**, *1*, e8.
[42] L. Daniault, M. Hanna, L. Lombard, Y. Zaouter, E. Mottay, D. Goular, P. Bourdon, F. Druon, P. Georges, *Opt. Lett.* **2011**, *36*, 621.
[43] H. Stark, J. Buldt, M. Müller, A. Klenke, J. Limpert, *Opt. Lett.* **2021**, *46*, 969.
[44] P. Zhou, Z. Liu, X. Wang, Y. Ma, H. Ma, X. Xu, S. Guo, *IEEE J. Sel. Top. Quantum Electron.* **2009**, *15*, 248.
[45] C. J. Corcoran, F. Durville, *Appl. Phys. Lett.* **2005**, *86*, 201118.
[46] B. He, Q. Lou, W. Wang, J. Zhou, Y. Zheng, J. Dong, Y. Wei, W. Chen, *Appl. Phys. Lett.* **2008**, *92*, 251115.
[47] H. Bruesselbach, D. C. Jones, M. S. Mangir, M. Minden, J. L. Rogers, **2005**, *30*, 1339.
[48] J. E. Rothenberg, *in Fiber Lasers V: Technology, Systems, and Applications*, SPIE, Bellingham, Washington, USA **2008**, pp. 222–230.
[49] D. V. Vysotsky, A. P. Napartovich, *Quantum Electron.* **2019**, *49*, 989.
[50] H. Fathi, M. Närhi, R. Gumenyuk, *Photonics* **2021**, *8*, 566.
[51] M. Wang, R.-Y. Zhang, L. Zhang, D. Wang, Q. Guo, Z.-Q. Zhang, C. T. Chan, *Phys. Rev. Lett.* **2021**, *126*, 067401.
[52] T. Fukui, Y. Hatsugai, H. Suzuki, *J. Phys. Soc. Jpn.* **2005**, *74*, 1674.
[53] C. Wang, H. Zhang, H. Yuan, J. Zhong, C. Lu, *Front. Optoelectron.* **2020**, *13*, 73.
[54] M. Z. Hasan, C. L. Kane, *Rev. Mod. Phys.* **2010**, *82*, 3045.
[55] G.-G. Liu, P. Zhou, Y. Yang, H. Xue, X. Ren, X. Lin, H. Sun, L. Bi, Y. Chong, B. Zhang, *Nat. Commun.* **2020**, *11*, 1873.
[56] A. Brignon, *Coherent Laser Beam Combining*, John Wiley & Sons, Ltd **2013**.
[57] X. Xie, M. Wei, Y. Yang, Y. Li, K. Lei, Z. Zhang, C. Wang, C. Zhong, L. Li, Z. Wang, W. E. I. Sha, E. Li, H. Xue, Z. Yang, L. Yuan, H. Chen, H. Lin, F. Gao, *Adv. Funct. Mater.* **2023**, *33*, 2302197.
[58] X.-D. Chen, X.-T. He, J.-W. Dong, *Laser Photonics Rev.* **2019**, *13*, 1900091.
[59] Z. Zhang, D. Liao, Y. Li, X. Xie, Y. Yang, K. Wang, Z. Dong, E. Li, H. Chen, F. Gao, *Laser Photonics Rev.* **2025**, *19*, 2400567.
[60] Y. Zhang, Q. Du, C. Wang, T. Fakhrul, S. Liu, L. Deng, D. Huang, P. Pintus, J. Bowers, C. A. Ross, J. Hu, L. Bi, *Optica* **2019**, *6*, 473.
[61] W. Yan, Y. Yang, S. Liu, Y. Zhang, S. Xia, T. Kang, W. Yang, J. Qin, L. Deng, L. Bi, *Optica* **2020**, *7*, 1555.